Journal of the Optical Society of America B

OPTICAL PHYSICS

Active THz metasurfaces for compact isolation

EVANGELOS ALMPANIS,[1,2,*] GRIGORIOS P. ZOUROS,[1,3] AND KOSMAS L. TSAKMAKIDIS[1,4]

[1]Section of Condensed Matter Physics, National and Kapodistrian University of Athens, Panepistimioupolis, GR-157 84 Athens, Greece
[2]Institute of Nanoscience and Nanotechnology, NCSR "Demokritos", Patriarchou Gregoriou and Neapoleos Street, Ag. Paraskevi, GR-153 10 Athens, Greece
[3]School of Electrical and Computer Engineering, National Technical University of Athens, GR-157 73 Athens, Greece
[4]e-mail: ktsakmakidis@phys.uoa.gr
*Corresponding author: ealmpanis@gmail.com

Received 27 April 2021; revised 7 July 2021; accepted 21 July 2021; posted 21 July 2021 (Doc. ID 430160); published 17 August 2021

Metasurfaces constitute an emerging technology, allowing for compact manipulation of all degrees of freedom of an incident lightwave. A key ongoing challenge in the design of these structures is how to allow for energy-efficient dynamic (active) operation, particularly for the polarization of incident light, which other standard devices typically cannot efficiently act upon. Here, we present a quasi-two-dimensional magneto-optic metasurface capable of simultaneously high-contrast on/off operation, as well as rotation of the polarization angle of a linearly polarized wave—that is, without converting the incident linear polarization to elliptical, which is normally particularly challenging. Furthermore, the device's operation is broadband, with a bandwidth of around 5 μm, and can be conveniently manipulated using an external magnetic bias. Our findings, corroborated using two different full-wave simulation approaches, may allow for functional metasurfaces operating in the terahertz (THz) regime, giving rise to robust, energy-efficient, and high-dynamic-range broadband isolation, to be used for a wealth of optoelectronic and communication applications.

https://doi.org/10.1364/JOSAB.430160

1. INTRODUCTION

Recently, there has been an increasing demand for devices operating in the terahertz (THz) band (0.1-10 THz), among others, due to their very promising applications in 5G/6G communication networks [1–3]. In this respect, structures such as THz photonic-crystal waveguides [4–6], metamaterials [7–11], gratings or patterned surfaces [12–14], magneto-dielectric metafilms [15], graphene plasmonics [16], structures for polarization switching [17], and multiplexing [18], as well as THz metasurfaces [19–21], have been investigated. Furthermore, research is focused on making such devices easily tunable by external agents [22,23]. For instance, thermally tunable THz photonic crystals and surfaces have been proposed [24,25]. However, the temperature-dependent tunability lacks the fast response, which is important for real-world applications.

To achieve fast active tuning, THz structures with electrical [26,27] or magnetical [28] tunability have been emerged. For instance, magnetically controlled THz directional scatterers [29,30] have been recently proposed. Furthermore, the class of magnetically active structures involves designs from THz magneto-photonic crystals [31,32] to non-reciprocal waveguides [33,34] and Faraday rotators [35–38] to topological insulators [39], with interesting abilities such as backscattering immunity [40], magnetically induced transparency [41], and non-reciprocal reflection [42]. A special class of Faraday rotators for THz radiation isolation is magneto-photonic metasurfaces [43–45] that combine ultra-thin width with increased Faraday rotation. We note here that an ideal Faraday isolator for linearly polarized light must transmit 100% of the incoming light and rotate the polarization plane by 45° [46,47]. However, an essential drawback in Faraday-active metasurfaces is the moderate or low transmission that hinders the total performance of magneto-optic isolators [48–55].

To overcome the problem of low transmission in ultra-thin Faraday isolators, in this paper, we propose a novel magneto-optic metasurface. This metasurface is composed of the strongly directional core-shell particles demonstrated in a recent publication of ours [56]. Now, inter-particle interactions and multiple scattering events, due to the lattice, result in highly transmittive Faraday isolators. Using full-wave finite element simulations by two independent commercial software, we seek strongly rotated linearly polarized transmitted light in such periodic arrays. Our results are supported by a consistent theoretical interpretation. The remainder of the paper is organized as follows: In Section 2.A, we examine the magneto-optical properties of the isolated core-shell particle. We show strong forward scattering of light in the presence of an experimentally reachable magnetic field. In Section 2.B, we use the core-shell particle described above as a building block for periodic arrangements of such. Transmission in accordance with Faraday rotation is investigated in such arrays, where magnetically switchable and tunable optical isolation is shown at THz frequencies. Finally, Section 3 concludes the paper.

2. RESULTS AND DISCUSSION

A. Isolated Core-Shell Scatterer

At first, we study the individual core-shell scatterer in air, shown in Fig. 1(a), that will serve as the building block of the magneto-optic surface. We note here that core-shell particles and arrays of such are possible using modern nano/micro-fabrication techniques [57–59]. This core-shell particle consists of a high-permittivity dielectric core with $\epsilon_{\rm core} = 20\epsilon_0$ (with ε_0 being the free space permittivity) of 14 μm radius, coated by a 20 μm radius InSb shell. We also consider an external magnetic field $\mathbf{B} = B\mathbf{z}$, as shown in Fig. 1(a). Upon magnetization, the InSb permittivity is described by a tensor of the form

$$\epsilon_{\rm InSb}(B) = \begin{pmatrix} \epsilon_1(B) & i\epsilon_2(B) & 0 \\ -i\epsilon_2(B) & \epsilon_1(B) & 0 \\ 0 & 0 & \epsilon_3 \end{pmatrix}. \quad (1)$$

The components of this tensor are complex functions of the frequency due to the dissipative and dispersive behavior of the material. In particular, $\epsilon_1(B) = \epsilon_0\epsilon_\infty\{1 - (\omega + iv)\omega_p^2/\omega/[(\omega + iv)^2 - \omega_c^2(B)]\}$, $\epsilon_2(B) = \epsilon_0\epsilon_\infty\{\omega_c(B)\omega_p^2/\omega/[(\omega + iv)^2 - \omega_c^2(B)]\}$, and $\epsilon_3 = \epsilon_0\epsilon_\infty[1 - \omega_p^2/\omega/(\omega + iv)]$ [60]. In the above relations, $\epsilon_\infty = 15.6$ accounts for interband transitions, $\omega_p = (N_e e^2/\epsilon_0/\epsilon_\infty/m^*)^{1/2} = 4\pi \times 10^{12}$ rad/s is the plasma angular frequency (with N_e the electron density, e the elementary charge, and $m^* = 0.0142 m_e$ the electron's effective mass, where m_e is the electron's rest mass), $\omega_c(B) = eB/m^*$ is the cyclotron angular frequency, and $v = 0.001\omega_p$ is the damping angular frequency associated with losses. Obviously, under zero external magnetization, InSb becomes isotropic with $\epsilon_1(0) = \epsilon_3$ and $\epsilon_2(0) = 0$.

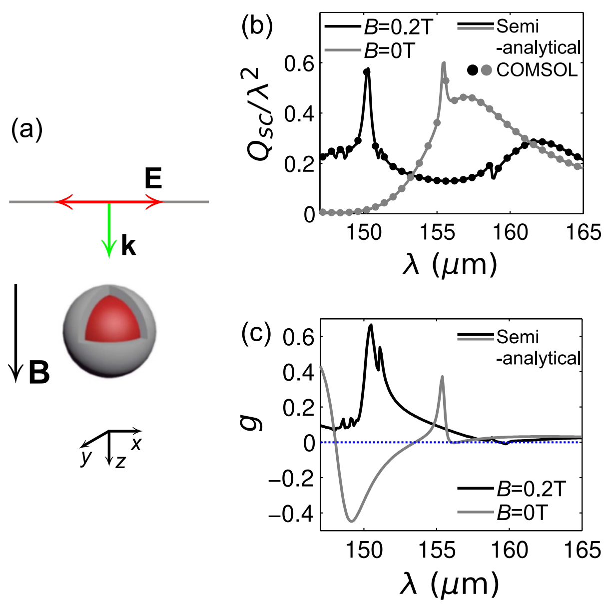

Fig. 1. (a) Schematics of the scatterer under consideration consisting of a high-index dielectric core of radius 14 μm and an indium antimonide (InSb) coating of thickness 6 μm. Linearly polarized light impinges along the z axis, while an external static magnetic field is parallel to the incident light. (b) Scattering cross section for external magnetic field $B = 0$T (gray curve) and $B = 0.2$T (black curve). (c) Asymmetry parameter defined in Eq. (3); the legends are the same as in (b).

The scatterer under consideration is illuminated by linearly polarized light, as shown in Fig. 1(a). The respective scattering cross section $Q_{\rm sc}$ is defined as the ratio of the scattered far-field power over the time-averaged incident power flow, i.e.,

$$Q_{\rm sc} = \frac{1}{|\mathbf{S}_{\rm inc}|} \oint \hat{\mathbf{n}} \cdot \mathbf{S}_{\rm sc} dS. \quad (2)$$

In Eq. (2), $\hat{\mathbf{n}}$ is the unit vector pointing outwards from (and normal to) the spherical surface of radius r, as $r \to \infty$, and $\mathbf{S}_{\rm sc}$ is the scattered far-field time-averaged power flow. Calculations for $Q_{\rm sc}$ have been performed using both our semi-analytical method described in full detail in [56], and the commercial finite element solver COMSOL.

Figure 1(b) depicts the corresponding $Q_{\rm sc}$ spectra versus the free space wavelength λ for $B = 0$T and $B = 0.2$T in the gray and black curves, respectively. We use an indicative value of the external magnetic field, close to those examined in Ref. [56], without any further optimization. As it is evident, the semi-analytical method and COMSOL are in excellent agreement. For the non-magnetized case, we see two resonant modes between 155–160 μm. Using typical multipolar decomposition for the scattered far-field, as the one implemented in [56], it comes out that the sharp resonance slightly above 155 μm corresponds to an electric quadrupole (EQ) mode, while the second resonance close to 175 μm corresponds to an electric dipole (ED) mode. Both of them are of plasmonic character. Obviously, the high-Q EQ mode is highly confined to the particle, as indicated by its high lifetime in the scattering cross section spectrum. In view of this, when placed within a lattice of similar spheres, the EQ modes will interact weakly among each other. On the other hand, the broader ED mode has low lifetime, and its field leaks in the space outside of the particle and thus will interact efficiently with modes of neighboring spheres to produce collective modes. Further insight can be obtained by employing the asymmetry parameter g [30] plotted in Fig. 1(c), i.e.,

$$g = \frac{\lambda^2}{\pi Q_{\rm sc}} \sum_{m=-\infty}^{\infty} \sum_{n=|m|}^{\infty} {\rm Re}\{(a_{mn})^* F_{mn} + (b_{mn})^* G_{mn}\}. \quad (3)$$

In Eq. (3), the term ($m = 0, n = 0$) is excluded from the summation, Re denotes the real part, a_{mn} and b_{mn} are the expansion coefficients of the scattered electric field expressed in the form of a multipolar decomposition [56], the asterisk denotes complex conjugation, and $F_{mn} = P_{mn}b_{mn} + Q_{mn}a_{m,n+1} + R_{mn}a_{m,n-1}$, $G_{mn} = P_{mn}a_{mn} + Q_{mn}b_{m,n+1} + R_{mn}b_{m,n-1}$, with $P_{mn} = m/n/(n+1)$, $Q_{mn} = [n(n+2)(n-m+1)(n+m+1)/(n+1)^2/(2n+1)/(2n+3)]^{1/2}$, and $R_{mn} = [(n-1)(n+1)(n-m)(n+m)/n^2/(2n-1)/(2n+1)]^{1/2}$. In particular, if $g < 0$, more radiation is scattered backwards, while when $g > 0$ the scattering is more forward-directed. g in Eq. (3) involves the expansion coefficients of the scattered electric field; therefore, it is computed by our semi-analytical method [56]. Observing Fig. 1(c), we conclude that for the non-magnetized case (gray curve) and for lower wavelengths, i.e., from 147–153 μm, the particle strongly backscatters the incident light. The scattering is forward directional only for a narrow region close to the EQ mode, while for higher wavelengths the scattering is not directional.

When the sphere is magnetized, the InSb shell becomes gyroelectric (optically anisotropic), which results in a far more different optical spectrum, as shown by the black curve in Fig. 1(b). Similar spectral features in almost identical scatterers have been extensively discussed in [30,56], and thus we will only review them briefly. Starting from lower wavelengths, we observe a sharp resonance close to 150 μm. In addition, from the corresponding g-parameter black curve of Fig. 1(c), this resonance is strongly directional, scattering light in the forward direction. This is a Zeeman split magneto-plasmonic resonance, due to the anisotropy induced by the magnetization [30,56,61]. Other Zeeman split modes also exist, which are not efficiently excited when light impinges along the magnetization axis, as discussed in [56]. In addition, a Fano-like asymmetric resonance [62] also appears in the spectral window of Fig. 1(b), close to 159 μm. One should keep in mind that, for wavelengths from 150–159 μm, the isolated particle, when magnetized, scatters light in the forward direction. The forward-scattering directionality in the particular bandwidth promises that an appropriate arrangement of such scatterers would result in a highly transmittive surface, since the optical characteristics of individual scatterers are often retained, or even enhanced, in periodic lattices of such [63].

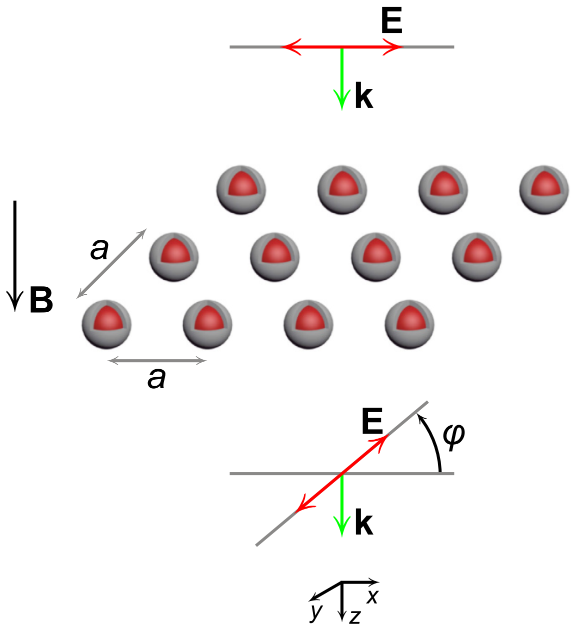

Fig. 2. (a) Graphical representation of the metasurface under consideration that constituted of a periodical arrangement (lattice constant $a = 70$ μm) of identical core-shell particles, as those discussed in Fig. 1. Linearly polarized light impinges normally, while an external static magnetic field is parallel to the incident light. The Faraday rotation angle φ lies in the xy plane.

B. Layer of Core-Shell Scatterers

We place core-shell particles, identical to the one studied in Section 2.A, in a square planar periodic arrangement of periodicity (lattice constant) a, as shown in Fig. 2. The incoming field impinges normally to the plane of the array and is linearly polarized. The applied external magnetic field B is co-parallel with incident light, i.e., along the z axis, as shown in Fig. 2, whereas the so called Faraday effect takes place by rotating the polarization plane of the transmitted light. We assume $\lambda > a$, hence no diffraction beams exist. The incident light is polarized in the x direction. In the non-magnetized case, the transmitted/reflected field is also polarized in the same direction. However, when the structure is magnetized, there are two (complex) transmission coefficients t_x, t_y, along the x and y axis, respectively, due to the Faraday effect. The total transmittance T is defined as $T = |t_x|^2 + |t_y|^2$, where, in general, the transmitted light is elliptically polarized. The respective Faraday rotation φ and ellipticity angle η are calculated by [64]

$$\varphi = \frac{1}{2}\tan^{-1}\frac{2\,\mathrm{Re}\{t_y/t_x\}}{1-|t_y/t_x|^2}, \tag{4}$$

$$\eta = \frac{1}{2}\sin^{-1}\frac{-2\,\mathrm{Im}\{t_y/t_x\}}{1+|t_y/t_x|^2}. \tag{5}$$

In cases where $\eta = 0$, the transmitted light is linearly polarized.

For $a = 70$ μm, we perform full-wave electrodynamic simulations using two commercial finite element solvers, COMSOL and High Frequency Structure Simulator (HFSS), to fully validate our results. The results are shown in Fig. 3. In Fig. 3(a), we depict the transmission spectra for $B = 0$T (gray curve) and $B = 0.2$T (black curve), while in Fig. 3(b) we plot the corresponding Faraday rotation and ellipticity angle for $B = 0.2$T (black solid and dashed curves). Obviously, the results from the two independent commercial software are in agreement in both Figs 3(a) and 3(b). At zero magnetization, the individual particles behave as typical metal-dielectric scatterers, exhibiting a strong reflective/absorbing band around 155 μm, as shown by the double-arrow blue dashed line. Such absorbing bands, or reflective for perfect electric conductors, are typical in lattices of metallic spherical particles or shells [65,66]. This strong interaction is primarily attributed to the significant overlap between the ED modes of the individual scatterers. At, 155 μm where transmittance is almost zero, at zero magnetic field, we plot the respective normalized electric-field profile of $\mathrm{Re}\{E_x\}/\max\{\mathrm{Re}\{E_x\}\}$ in Fig. 3(c)/top. From this plot, it is evident that the field below the metasurface is almost null. This transmittance-blocking band is interrupted by a narrow-band transmitting channel due to a weak interaction between the quadrupolar modes of the individual scatterers.

By switching on the magnetization, the surface of Fig. 2 is mostly transmittive, with the exception of wavelengths smaller than 149 μm and greater than 159 μm. The transmittance dropping close to 150 μm and 151 μm is associated with collective magneto-plasmonic bands associated with the weakly interacting Zeeman split modes. The band around 159 μm is associated with the Fano resonance of the individual scatterer. In the intermediate region, i.e., between 151 μm and 159 μm, we observe increased transmittance accompanied by an increased Faraday rotation (φ angle), as shown in Fig. 3(b) by

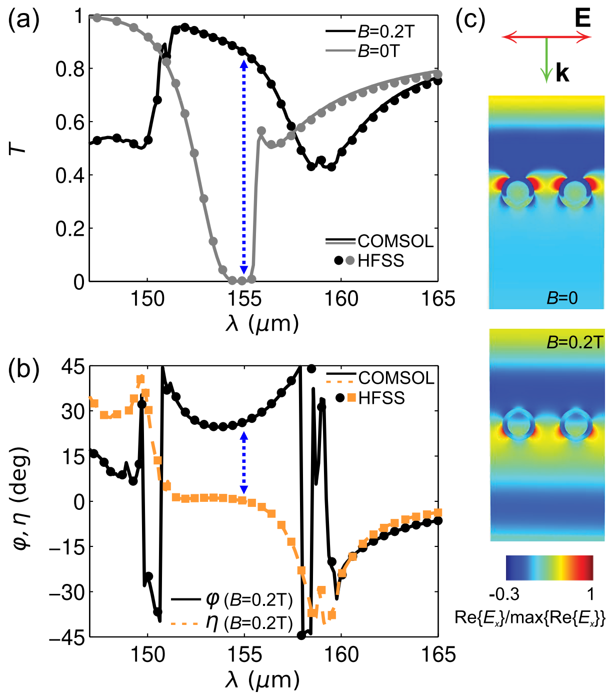

Fig. 3. (a) Transmission spectra for external magnetic field $B = 0\text{T}$ (gray curve) and $B = 0.2\text{T}$ (black curve). The double-arrow blue dashed line depicts the strong reflection/absorption around 155 μm. (b) Corresponding Faraday rotation and ellipticity angle for $B = 0.2\text{T}$. The double-arrow blue dashed line at 155 μm depicts the location where the ellipticity angle η becomes zero. For $B = 0\text{T}$, both angles are zero. (c) Normalized field profiles. Top: $B = 0\text{T}$; bottom: $B = 0.2\text{T}$.

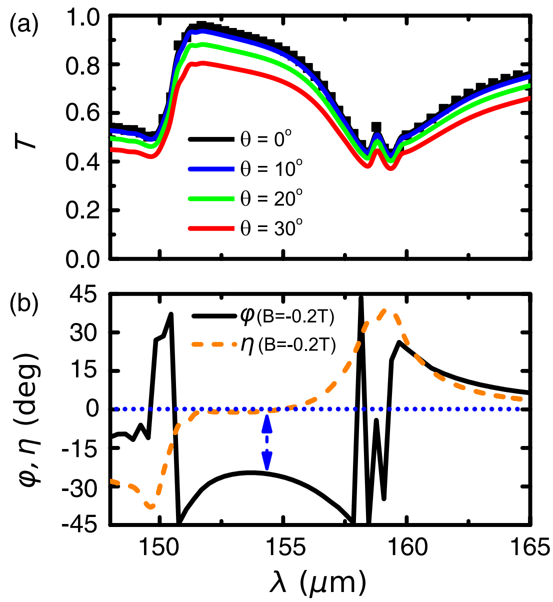

Fig. 4. (a) Transmission spectra for the configuration of Fig. 3(a) at $B = 0.2\text{T}$ for incident light at an angle θ with respect to the z axis. The black solid line corresponds to $\theta = 0°$, the blue line corresponds to $\theta = 10°$, the green line corresponds to $\theta = 20°$, while the red line corresponds to $\theta = 30°$. With square symbols, we show the respective transmission at normal incidence of light ($\theta = 0°$) for the reversed magnetic-field case, i.e., $B = -0.2\text{T}$. (b) Faraday rotation and ellipticity angles at normal incidence of light for the reversed magnetic-field case, i.e., $B = -0.2\text{T}$. The dashed double-arrow line depicts the location where η becomes zero.

the black solid curve. Moreover, at 155 μm, the ellipticity angle η [dashed curve in Fig. 3(b)] becomes zero, which means that the transmitted light is linearly polarized. The normalized field profile at the above-mentioned wavelength, pointed out with the double-arrow blue dashed line, is shown in Fig. 3(c)/bottom. Noteworthy, an almost-zero ellipticity angle is preserved over a broad wavelength band, as shown in Fig. 3(b). Such a property is very promising for real-world applications, such as magneto-photonic isolators [43–45]. Therefore, our attention is focused on the linearly polarized output light.

Next, we discuss the robustness of the metasurface performance under off-normal incidence of light. In Fig. 4(a), we show the transmission spectrum for angles of incidence from 0° to 30°. The case of normal incidence ($\theta = 0°$) is already shown in Fig. 3(a). In Fig. 4(a), we observe that for $\theta = 10°$ (blue line), the transmittance remains almost unchanged. This calculation indicates that the metasurface is almost immune to small deviations of the angle of incidence θ (0°–10°). By further increasing θ, we observe a respective reduction of the maximum transmission. However, even for $\theta = 30°$ the transmission remains above 0.75, which is still high enough for applications. Another aspect worth noting is the non-reciprocal behavior of the magnetized metasurface. In the Faraday configuration, which is the one discussed here, the external magnetic field can be either parallel or anti-parallel to the incidence of light. Up to now, we discussed the parallel case. By changing the sign of the external magnetic field, we denote that the field is anti-parallel, i.e., along the negative z direction. The respective transmittance for $B = -0.2\text{T}$, at normal incidence, is shown with square symbols in Fig. 4(a). As shown, the transmittance of the anti-parallel (reversed) magnetic-field case is the same as that of the parallel one. However, by looking at the respective Faraday rotation and ellipticity angles in Fig. 4(b), we observe that they have opposite signs with respect to the parallel case. The reason behind this is the non-reciprocity induced by the external magnetization, which induces opposite signs to the respective Faraday rotation angles.

To further highlight the performance of the metasurface, we calculate the respective transmittance and Faraday rotation characteristics of an InSb slab. We consider two cases: one for slab thickness $d = 12$ μm and one for $d = 40$ μm. The first case corresponds to an (roughly) effective thickness of the InSb coating only. The second case corresponds to the total thickness of the metasurface. The transmittance and Faraday rotation of the metasurface should exceed those of a respective homogeneous magneto-optic (InSb) slab. In Fig. 5(a), we show the transmittance at $B = 0\text{T}$ (gray line) and $B = 0.2$ T (black line) for the InSb slab with $d = 12$ μm. As is evident, in the wavelength region of interest, the transmittance for the unmagnetized slab varies from almost unity (at lower wavelengths) to roughly 0.4 (at higher wavelengths). By switching on the external magnetic field ($B = 0.2\text{T}$), the transmittance ranges roughly from 0.6 to 0.5, which means it is significantly lower than the respective transmittance of our metasurface close to its operation wavelength (152–155 μm). Similarly, in Fig. 5(b), we show the transmittance at $B = 0\text{T}$ (gray line) and $B = 0.2\text{T}$ (black line) for the InSb slab with $d = 40$ μm.

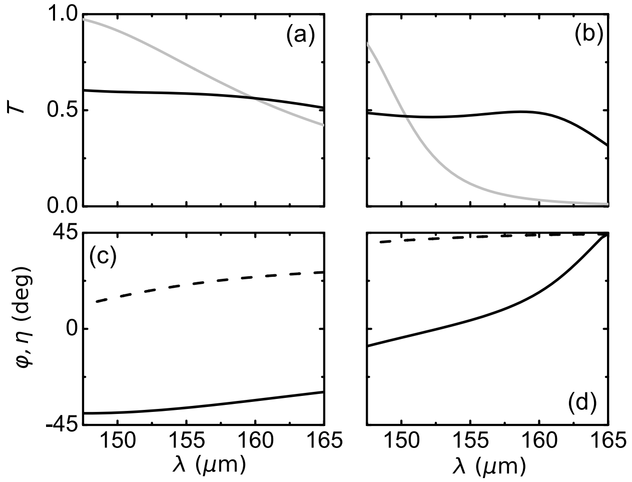

Fig. 5. (a) Transmittance at $B = 0T$ (gray line) and $B = 0.2T$ (black line) for an air-located homogeneous InSb slab with $d = 12$ μm. (b) Transmittance at $B = 0T$ (gray line) and $B = 0.2T$ (black line) for an air-located homogeneous InSb slab with $d = 40$ μm. (c) Faraday rotation angle (solid line) and ellipticity angle (dashed line) for the magnetized slab ($B = 0.2T$) with $d = 12$ μm. (d) Faraday rotation angle (solid line) and ellipticity angle (dashed line) for the magnetized slab ($B = 0.2T$) with $d = 40$ μm.

Now, the transmittance of the unmagnetized slab drops abruptly at higher wavelengths, although the transmittance of the magnetized slab remains close to 0.5 in the wavelength region of interest, i.e., 152–155 μm. We should keep in mind that in both cases our metasurface exhibits significantly higher transmittance (close to 0.85 in the wavelength region of interest). Next, we examine the Faraday rotation and ellipticity angle in such homogeneous-slab cases. Particularly, in Fig. 5(c), we show the corresponding Faraday rotation (solid line) and ellipticity (dashed line) angles for the slab with $d = 12$ μm. Although the Faraday rotation angle reaches almost $-40°$, the ellipticity angle significantly deviates from 0°. This means that the transmitted light is elliptically polarized and therefore does not meet our goal for linearly polarized light in the output of our polarization rotator/isolator. In the same respect, the ellipticity angle for the slab with $d = 40$ μm, shown in Fig. 5(d) with a dashed line, is close to 45°, which leads to the conclusion that the transmitted light is almost circularly polarized. In view of the above, our designed magnetically active metasurface significantly outperforms the corresponding homogeneous slab made of the same magnetically active material.

The metasurface discussed in Figs. 3 and 4 consists of core-shell particles with inner radius $R_1 = 14$ μm and outer radius $R_1 = 20$ μm arranged in a square arrangement of lattice constant a at $B = 0.2T$. Since these parameters have not been optimized, it is obvious that these degrees of freedom can be tuned in order to approach perfect isolation, i.e., $\varphi = 45°$ and $T = 100\%$. At first, we keep the lattice constant a and the inner radius R_1 fixed and change the outer radius R_2, as shown in Figs. 6(a) and 6(b). In Fig. 6(a), we show the wavelength λ_0, at which output polarization is linear ($\eta = 0$). In this case, λ_0 shifts to higher wavelengths as R_2 increases. In Fig. 6(b), we plot the respective transmittance T and Faraday rotation angle φ at λ_0 versus R_2. We observe that, by increasing the particle's

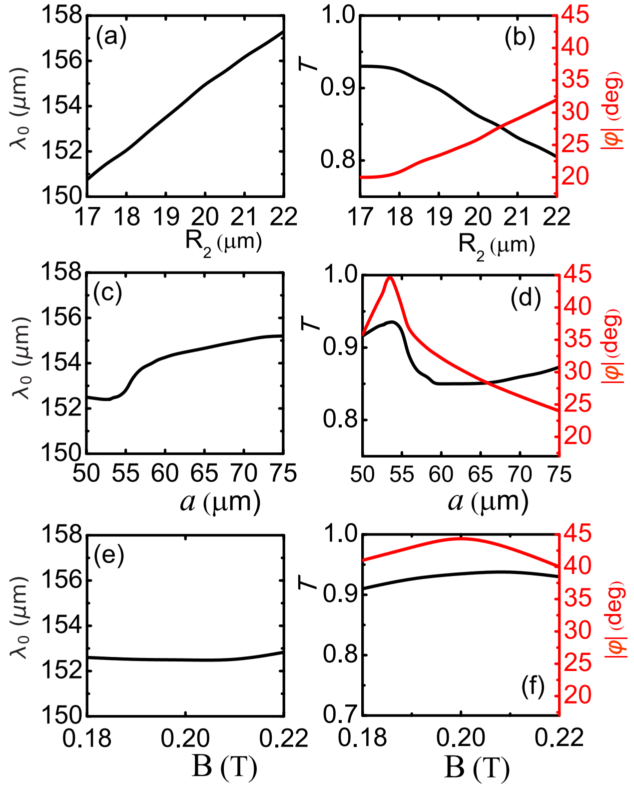

Fig. 6. (a) Wavelength λ_0 versus R_2 for the zero ellipticity angle for a metasurface with lattice constant $a = 70$ μm. (b) Left axis/black curve: transmittance versus R_2 for $B = 0.2T$ at wavelength λ_0. Right axis/red curve: Faraday rotation angle versus R_2 at λ_0. (c) Wavelength λ_0 versus a for zero ellipticity angle for a metasurface with $R_2 = 20$ μm. (d) Left axis/black curve: transmittance versus a for $B = 0.2T$ at wavelength λ_0. Right axis/red curve: Faraday rotation angle versus a at λ_0. (e) Wavelength λ_0 versus B for zero ellipticity angle for a metasurface with lattice constant $a = 53.5$ μm and $R_2 = 20$ μm. (f) Left axis/black curve: transmittance versus B at wavelength λ_0. Right axis/red curve: Faraday rotation angle versus B at λ_0.

outer radius R_2, the transmittance at λ_0 is decreased, while the respective Faraday rotation angle is increased. Such a behavior indicates a trade off between transmittance and Faraday rotation, when changing R_2; the optimization of φ results in a loss in transmitted light. Therefore, we keep R_2 at 20 μm in the next optimization study. In Fig. 6(c), we plot λ_0 versus the lattice constant a, while in Fig. 6(d) the respective transmittance T and Faraday rotation angle φ is at λ_0. For $a \geqslant 60$ μm, the transmittance increases while φ decreases. Obviously, when the lattice becomes more sparse (by increasing a), the transmittance is increased. The increment in T is followed by a decrement in φ, because light interacts less with the individual scatterers. However, for $a \leqslant 60$ μm, there is a peak for both T and φ at $a = 53.5$ μm, with $T = 94\%$ and $\varphi = 45°$. These values indicate a very efficient Faraday isolator, capable of real-world applications. Finally, the robustness of the metasurface's performance versus small deviations of the external magnetic field is examined. In Fig. 6(e), we plot the change in λ_0 versus B. We observe that λ_0 remains almost the same under small deviations of B. Similarly, in Fig. 6(f), we observe that both φ and T retain their high values irrespective of the precise value of B.

3. CONCLUSIONS

In summary, we have presented the design and full-wave analysis of a magnetically switchable metasurface allowing for attaining robust and high-contrast isolation at THz wavelengths. Our device was made of high-index spherical dielectric metaparticles, cladded with a magnetized semiconductor, InSb. Upon application of an external magnetic field, the device can almost be perfectly switched on and off over a relatively broad range of wavelengths. Crucially, the device does not alter the linear polarization of the incident lightwave despite the fact that its individual meta-atoms, when on their own, typically do. The straightforward design of the structure and the combined functionalities it provides may make it appealing for a range of applications in optoelectronic and communication systems.

Funding. Hellenic Foundation for Research and Innovation (1819); General Secretariat for Research and Technology (1819).

Disclosures. The authors declare no conflicts of interest.

Data Availability. The data that support the findings of this study are available from the corresponding authors upon request.

REFERENCES

1. J. F. O'Hara, S. Ekin, W. Choi, and I. Song, "A perspective on terahertz next-generation wireless communications," Technologies **7**, 43 (2019).
2. Z. Zhang, Y. Xiao, Z. Ma, M. Xiao, Z. Ding, X. Lei, G. K. Karagiannidis, and P. Fan, "6G wireless networks: vision, requirements, architecture, and key technologies," IEEE Veh. Technol. Mag. **14**(3), 28–41 (2019).
3. M. Giordani, M. Polese, M. Mezzavilla, S. Rangan, and M. Zorzi, "Toward 6G networks: use cases and technologies," IEEE Commun. Mag. **58**(3), 55–61 (2020).
4. Z. Li, Y. Zhang, and B. Li, "Terahertz photonic crystal switch in silicon based on self-imaging principle," Opt. Express **14**, 3887–3892 (2006).
5. S. Matloub, M. Hosseinzadeh, and A. Rostami, "The narrow band THz filter in metallic photonic crystal slab framework: design and investigation," Optik **125**, 6545–6549 (2014).
6. F. Gardes, K. Tsakmakidis, D. Thomson, G. Reed, G. Mashanovich, O. Hess, and D. Avitabile, "Micrometer size polarisation independent depletion-type photonic modulator in silicon on insulator," Opt. Express **15**, 5879–5884 (2007).
7. H.-T. Chen, J. F. O'Hara, A. K. Azad, and A. J. Taylor, "Manipulation of terahertz radiation using metamaterials," Laser Photon. Rev. **5**, 513–533 (2011).
8. L. Huang, D. R. Chowdhury, S. Ramani, M. T. Reiten, S.-N. Luo, A. J. Taylor, and H.-T. Chen, "Experimental demonstration of terahertz metamaterial absorbers with a broad and flat high absorption band," Opt. Lett. **37**, 154–156 (2012).
9. T. Wang, H. Zhang, Y. Zhang, Y. Zhang, and M. Cao, "Tunable bifunctional terahertz metamaterial device based on Dirac semimetals and vanadium dioxide," Opt. Express **28**, 17434–17448 (2020).
10. K. Tsakmakidis and O. Hess, "Extreme control of light in metamaterials: complete and loss-free stopping of light," Phys. B **407**, 4066–4069 (2012).
11. K. Tsakmakidis, O. Reshef, E. Almpanis, G. Zouros, E. Mohammadi, D. Saadat, F. Sohrabi, N. Fahimi-Kashani, D. Etezadi, R. Boyd, and H. Altug, "Ultrabroadband 3D invisibility with fast-light cloaks," Nat. Commun. **10**, 4859 (2019).
12. J. G. Rivas, C. Janke, P. H. Bolivar, and H. Kurz, "Transmission of THz radiation through InSb gratings of subwavelength apertures," Opt. Express **13**, 847–859 (2005).
13. A. K. Azad, J. F. O'Hara, R. Singh, H.-T. Chen, and A. J. Taylor, "A review of terahertz plasmonics in subwavelength holes on conducting films," IEEE J. Sel. Top. Quantum Electron. **19**, 8400416 (2012).
14. H. Zhao, X. Wang, J. He, J. Guo, J. Ye, Q. Kan, and Y. Zhang, "High-efficiency terahertz devices based on cross-polarization converter," Sci. Rep. **7**, 17882 (2017).
15. C. L. Holloway, P. Kabos, M. A. Mohamed, E. F. Kuester, J. A. Gordon, M. D. Janezic, and J. Baker-Jarvis, "Realisation of a controllable metafilm/metasurface composed of resonant magnetodielectric particles: measurements and theory," IET Microw. Antennas Propag. **4**, 1111–1122 (2010).
16. T. Low and P. Avouris, "Graphene plasmonics for terahertz to mid-infrared applications," ACS Nano **8**, 1086–1101 (2014).
17. L. Cong, Y. K. Srivastava, H. Zhang, X. Zhang, J. Han, and R. Singh, "All-optical active THz metasurfaces for ultrafast polarization switching and dynamic beam splitting," Light Sci. Appl. **7**, 28 (2018).
18. B. Li, X. Li, R. Zhao, G. Wang, W. Han, B. Zhao, L. Huang, Y. Zhang, Y. Lu, and L. Jiang, "Polarization multiplexing terahertz metasurfaces through spatial femtosecond laser-shaping fabrication," Adv. Opt. Mater. **8**, 2000136 (2020).
19. J. A. Burrow, R. Yahiaoui, A. Sarangan, I. Agha, J. Mathews, and T. A. Searles, "Polarization-dependent electromagnetic responses of ultrathin and highly flexible asymmetric terahertz metasurfaces," Opt. Express **25**, 32540–32549 (2017).
20. S. Banerjee, C. Amith, D. Kumar, G. Damarla, A. K. Chaudhary, S. Goel, B. P. Pal, and D. R. Chowdhury, "Ultra-thin subwavelength film sensing through the excitation of dark modes in THz metasurfaces," Opt. Commun. **453**, 124366 (2019).
21. W. Xu, L. Xie, J. Zhu, L. Tang, R. Singh, C. Wang, Y. Ma, H.-T. Chen, and Y. Ying, "Terahertz biosensing with a graphene-metamaterial heterostructure platform," Carbon **141**, 247–252 (2019).
22. T. J. Arruda, A. S. Martinez, and F. A. Pinheiro, "Electromagnetic energy and negative asymmetry parameters in coated magneto-optical cylinders: applications to tunable light transport in disordered systems," Phys. Rev. B **94**, 033825 (2016).
23. S. Lepeshov, A. Krasnok, and A. Alù, "Nonscattering-to-superscattering switch with phase-change materials," ACS Photon. **6**, 2126–2132 (2019).
24. B. K. Singh and P. C. Pandey, "Tunable temperature-dependent THz photonic bandgaps and localization mode engineering in 1D periodic and quasi-periodic structures with graded-index materials and InSb," Appl. Opt. **57**, 8171–8181 (2018).
25. H. Luo and Y. Cheng, "Thermally tunable terahertz metasurface absorber based on all dielectric indium antimonide resonator structure," Opt. Mater. **102**, 109801 (2020).
26. Z. Miao, Q. Wu, X. Li, Q. He, K. Ding, Z. An, Y. Zhang, and L. Zhou, "Widely tunable terahertz phase modulation with gate-controlled graphene metasurfaces," Phys. Rev. X **5**, 041027 (2015).
27. Z. Wu, Y. Ra'di, and A. Grbic, "Tunable metasurfaces: a polarization rotator design," Phys. Rev. X **9**, 011036 (2019).
28. F. Fan, S. Chen, and S.-J. Chang, "A review of magneto-optical microstructure devices at terahertz frequencies," IEEE J. Sel. Top. Quantum Electron. **23**, 8500111 (2016).
29. M. Liu, C. Zhao, and B. Wang, "Active tuning of directional scattering by combining magneto-optical effects and multipolar interferences," Nanoscale **10**, 18282–18290 (2018).
30. G. P. Zouros, G. D. Kolezas, E. Almpanis, K. Baskourelos, T. P. Stefański, and K. L. Tsakmakidis, "Magnetic switching of Kerker scattering in spherical microresonators," Nanophotonics **9**, 4033–4041 (2020).
31. F. Fan, Z. Guo, J.-J. Bai, X.-H. Wang, and S.-J. Chang, "Magnetic photonic crystals for terahertz tunable filter and multifunctional polarization controller," J. Opt. Soc. Am. B **28**, 697–702 (2011).
32. F. Fan, S.-J. Chang, C. Niu, Y. Hou, and X.-H. Wang, "Magnetically tunable silicon-ferrite photonic crystals for terahertz circulator," Opt. Commun. **285**, 3763–3769 (2012).
33. B. Hu, Q. J. Wang, and Y. Zhang, "Broadly tunable one-way terahertz plasmonic waveguide based on nonreciprocal surface magneto plasmons," Opt. Lett. **37**, 1895–1897 (2012).
34. K. Tsakmakidis, L. Shen, S. Schulz, X. Zheng, J. Upham, X. Deng, H. Altug, A. Vakakis, and R. Boyd, "Breaking Lorentz reciprocity to overcome the time-bandwidth limit in physics and engineering," Science **356**, 1260–1264 (2017).

35. A. Shuvaev, G. Astakhov, A. Pimenov, C. Brüne, H. Buhmann, and L. Molenkamp, "Giant magneto-optical Faraday effect in HgTe thin films in the terahertz spectral range," Phys. Rev. Lett. **106**, 107404 (2011).
36. T. Arikawa, X. Wang, A. A. Belyanin, and J. Kono, "Giant tunable Faraday effect in a semiconductor magneto-plasma for broadband terahertz polarization optics," Opt. Express **20**, 19484–19492 (2012).
37. T. Arikawa, Q. Zhang, L. Ren, A. A. Belyanin, and J. Kono, "Review of anisotropic terahertz material response," J. Infrared, Millimeter, Terahertz Waves **34**, 724–739 (2013).
38. T.-F. Li, Y.-L. Li, Z.-Y. Zhang, Q.-H. Yang, F. Fan, Q.-Y. Wen, and S.-J. Chang, "Terahertz Faraday rotation of magneto-optical films enhanced by helical metasurface," Appl. Phys. Lett. **116**, 251102 (2020).
39. X. Li, K. Yoshioka, M. Xie, I. G. Timothy Noe, W. Lee, N. M. Peraca, W. Gao, T. Hagiwara, Ø. S. Handegård, and L.-W. Nien, "Terahertz Faraday and Kerr rotation spectroscopy of $Bi_{1-x}Sb_x$ films in high magnetic fields up to 30 tesla," Phys. Rev. B **100**, 115145 (2019).
40. Z. Wang, Y. Chong, J. D. Joannopoulos, and M. Soljačić, "Observation of unidirectional backscattering-immune topological electromagnetic states," Nature **461**, 772–775 (2009).
41. X. Wang, A. Belyanin, S. Crooker, D. Mittleman, and J. Kono, "Interference-induced terahertz transparency in a semiconductor magneto-plasma," Nat. Phys. **6**, 126–130 (2010).
42. S. Lin, S. Silva, J. Zhou, and D. Talbayev, "A one-way mirror: high-performance terahertz optical isolator based on magnetoplasmonics," Adv. Opt. Mater. **6**, 1800572 (2018).
43. S. Chen, F. Fan, X. He, M. Chen, and S. Chang, "Multifunctional magneto-metasurface for terahertz one-way transmission and magnetic field sensing," Appl. Opt. **54**, 9177–9182 (2015).
44. S. Chen, F. Fan, X. Wang, P. Wu, H. Zhang, and S. Chang, "Terahertz isolator based on nonreciprocal magneto-metasurface," Opt. Express **23**, 1015–1024 (2015).
45. F. Fan, S.-T. Xu, X.-H. Wang, and S.-J. Chang, "Terahertz polarization converter and one-way transmission based on double-layer magneto-plasmonics of magnetized InSb," Opt. Express **24**, 26431–26443 (2016).
46. M. Zamani, M. Ghanaatshoar, and H. Alisafaee, "Adjustable magneto-optical isolators with high transmittance and large Faraday rotation," J. Opt. Soc. Am. B **28**, 2637–2642 (2011).
47. M. Zamani and M. Ghanaatshoar, "Adjustable magneto-optical isolators with flat-top responses," Opt. Express **20**, 24524–24535 (2012).
48. V. Dmitriev, F. Paixão, and M. Kawakatsu, "Enhancement of Faraday and Kerr rotations in three-layer heterostructure with extraordinary optical transmission effect," Opt. Lett. **38**, 1052–1054 (2013).
49. V. Belotelov, L. Doskolovich, V. Kotov, E. Bezus, D. Bykov, and A. Zvezdin, "Faraday effect enhancement in metal-dielectric plasmonic systems," Proc. SPIE **6581**, 65810S (2007).
50. J. Y. Chin, T. Steinle, T. Wehlus, D. Dregely, T. Weiss, V. I. Belotelov, B. Stritzker, and H. Giessen, "Nonreciprocal plasmonics enables giant enhancement of thin-film Faraday rotation," Nat. Commun. **4**, 1599 (2013).
51. G. Armelles, A. Cebollada, A. Garca-Martn, and M. U. González, "Magnetoplasmonics: combining magnetic and plasmonic functionalities," Adv. Opt. Mater. **1**, 10–35 (2013).
52. C. Lei, L. Chen, Z. Tang, D. Li, Z. Cheng, S. Tang, and Y. Du, "Enhancement of magneto-optical Faraday effects and extraordinary optical transmission in a tri-layer structure with rectangular annular arrays," Opt. Lett. **41**, 729–732 (2016).
53. E. Almpanis, P.-A. Pantazopoulos, N. Papanikolaou, V. Yannopapas, and N. Stefanou, "Metal-nanoparticle arrays on a magnetic garnet film for tunable plasmon-enhanced Faraday rotation," J. Opt. Soc. Am. B **33**, 2609–2616 (2016).
54. E. Almpanis, P. Pantazopoulos, N. Papanikolaou, V. Yannopapas, and N. Stefanou, "A birefringent etalon enhances the Faraday rotation of thin magneto-optical films," J. Opt. **19**, 075102 (2017).
55. A. Christofi, Y. Kawaguchi, A. Alù, and A. B. Khanikaev, "Giant enhancement of Faraday rotation due to electromagnetically induced transparency in all-dielectric magneto-optical metasurfaces," Opt. Lett. **43**, 1838–1841 (2018).
56. G. P. Zouros, G. D. Kolezas, E. Almpanis, and K. L. Tsakmakidis, "Three-dimensional giant invisibility to superscattering enhancement induced by Zeeman-split modes," ACS Photon. **8**, 1407–1412 (2021).
57. K. P. Velikov, A. Moroz, and A. van Blaaderen, "Photonic crystals of core-shell colloidal particles," Appl. Phys. Lett. **80**, 49–51 (2002).
58. A. M. El-Toni, M. A. Habila, J. P. Labis, Z. A. Alothman, M. Alhoshan, A. A. Elzatahry, and F. Zhang, "Design, synthesis and applications of core–shell, hollow core, and nanorattle multifunctional nanostructures," Nanoscale **8**, 2510–2531 (2016).
59. F. M. Galogahi, Y. Zhu, H. An, and N.-T. Nguyen, "Core-shell microparticles: generation approaches and applications," J. Sci.: Adv. Mater. Devices **5**, 417–435 (2020).
60. K. L. Tsakmakidis, L. Shen, S. A. Schulz, X. Zheng, J. Upham, X. Deng, H. Altug, A. F. Vakakis, and R. W. Boyd, "Breaking Lorentz reciprocity to overcome the time-bandwidth limit in physics and engineering," Science **356**, 1260–1264 (2017).
61. E. Almpanis, "Dielectric magnetic microparticles as photomagnonic cavities: enhancing the modulation of near-infrared light by spin waves," Phys. Rev. B **97**, 184406 (2018).
62. F. Hao, Y. Sonnefraud, P. V. Dorpe, S. A. Maier, N. J. Halas, and P. Nordlander, "Symmetry breaking in plasmonic nanocavities: subradiant LSPR sensing and a tunable Fano resonance," Nano Lett. **8**, 3983–3988 (2008).
63. E. Panagiotidis, E. Almpanis, N. Stefanou, and N. Papanikolaou, "Multipolar interactions in Si sphere metagratings," J. Appl. Phys. **128**, 093103 (2020).
64. H. Kato, T. Matsushita, A. Takayama, M. Egawa, K. Nishimura, and M. Inoue, "Theoretical analysis of optical and magneto-optical properties of one-dimensional magnetophotonic crystals," J. Appl. Phys. **93**, 3906–3911 (2003).
65. N. Papanikolaou, "Optical properties of metallic nanoparticle arrays on a thin metallic film," Phys. Rev. B **75**, 235426 (2007).
66. C. Tserkezis, G. Gantzounis, and N. Stefanou, "Collective plasmonic modes in ordered assemblies of metallic nanoshells," J. Phys.: Condens. Matter **20**, 075232 (2008).